Astron. Astrophys. 359, 651–662 (2000)

ASTRONOMY AND ASTROPHYSICS

Circumstellar dust shells around long-period variables

VIII. CO infrared line profiles from dynamical models for C-stars

J.M. Winters[1,2], **J.J. Keady**[3], **A. Gauger**[4], **and P.V. Sada**[5]

[1] Max-Planck-Institut für Radioastronomie, Auf dem Hügel 69, 53121 Bonn, Germany
[2] Technische Universität Berlin, Institut für Astronomie und Astrophysik, PN 8-1, Hardenbergstrasse 36, 10623 Berlin, Germany
[3] Los Alamos National Laboratory, Theoretical Division, Group T–4, MS B268, Los Alamos, NM 87545, USA
[4] Fachhochschule Fulda, Marquardstrasse 35, 36039 Fulda, Germany
[5] Universidad de Monterrey, Departamento de Física y Matemáticas, Av. Moromes Prieto 4500 Pte., Garza García, N.L., 66238 México

Received 16 February 2000 / Accepted 26 April 2000

Abstract. We present simplified non-LTE radiative transfer calculations for CO (v 0-1) fundamental and (v 0-2) overtone lines, using the structure of dynamical models for dust shells around carbon-rich long-period variables, which result from a consistent treatment of hydro- and thermodynamics, radiative transfer, chemistry and carbon grain formation.

Owing to the saturation of the fundamental band absorption cores the most useful information is provided by the P-Cygni emission component, which can be used to constrain the dust optical depth in the $5\,\mu$m region. The first overtone lines clearly reflect the shocked, layered structure of the inner shell region by showing a multi-component structure of the profiles. At least the lines of higher rotational excitation ($J_l > 10$) are not saturated even for mass loss rates of the order of $10^{-5} M_\odot \mathrm{yr}^{-1}$ and thus can be used to constrain the mass loss rate. Furthermore, the dynamics of the dust formation process is reflected in the temporal evolution of the synthetic CO first overtone line profiles resulting from the models. The formation of a new dust layer in the inner shell region leads to a secondary (low velocity) absorption component which evolves on the time scale of a dust formation event, usually longer than the pulsation period of the star.

The synthetic overtone line profiles calculated on the basis of one dust shell model resemble the time variations of corresponding lines in the observed high resolution CO line spectra of the carbon-Mira IRC +10216, which thereby are interpreted as result of a dust formation event taking place on a time scale of $\approx$ 10 yr corresponding to 6 pulsation periods of the star. However, the calculated fundamental line absorption cores are broader than observed and the first overtone line strengths are too high, indicating that the density and thus probably the mass loss rate of the model is too high by a factor of about 3 and should be closer to the value of $1\,10^{-5}\,M_\odot \mathrm{yr}^{-1}$ given for IRC +10216 in the literature.

Key words: hydrodynamics – line: profiles – stars: circumstellar matter – stars: individual: IRC +10216 – stars: AGB and post-AGB – stars: winds, outflows

Send offprint requests to: J.M. Winters (jwinters@mpifr-bonn.mpg.de)

1. Introduction

Almost all Miras and most long–period variables (LPVs) are highly evolved low and intermediate mass stars located on the Asymptotic Giant Branch (AGB). These objects are large amplitude pulsators with typical periods of the order of $P \approx 1$ yr, high luminosities $L_* \approx 10^4 \mathrm{L}_\odot$, low effective temperatures $T_* \leq 3000$ K and high mass loss rates up to $\dot{M} \approx 10^{-4} \mathrm{M}_\odot \mathrm{yr}^{-1}$ (e.g. Habing 1996). The outflows from these cool stars are sites of copious grain formation, which is sometimes so effective, that the circumstellar dust shell (CDS) totally obscures the central object. In fact, these shells are considered to be the major sources for the replenishment of the interstellar medium with processed material, in particular in the form of complex molecules and of solid dust particles (e.g. Gehrz 1989).

These high mass loss winds cannot be a long-lasting phenomenon, since the stars themselves, when reaching the AGB, typically have masses of the order of one solar mass. Therefore, this high mass loss has a profound impact on the final evolutionary phase of the mass losing star, thereby producing the remaining Planetary Nebula or even single, thin detached shells (cf. Schröder et al. 1998, 1999)

To study the structure and dynamics of such CDS, the CO molecule is an especially well suited diagnostic probe. It is one of the most abundant species, both, in oxygen–rich and in carbon–rich objects. Due to its stability it forms already at high temperatures deep in the photosphere. In the subsequent outflow it remains relatively chemically inert out to large distances, thus, covering the whole range of physical conditions in the CDS. Its infrared and microwave spectrum is fairly simple, and line positions and oscillator strengths are well determined.

Probably the best studied representative of its class is the bright, carbon–rich, infrared Mira IRC +10216, which has been observed at many wavelengths with significant spectral and spatial resolution since its discovery by Neugebauer & Leighton (1969). The combined information obtained from the spectral energy distribution, molecular line spectra, brightness profiles and spatial spectra yields strong constraints on the properties of the CDS around IRC +10216, such as the flow velocity, the

temperature and density distribution of the gas, the gas phase chemistry and the molecular composition and its distribution (e.g. Groenewegen et al. 1998, Groenewegen 1997, Crosas & Menten 1997, Jura 1994, Winters et al. 1994a, Cherchneff et al. 1993, Keady & Ridgway 1993, Keady et al. 1988).

Keady and his collaborators performed detailed modeling of the infrared molecular line profiles of the CO molecule using a semi-empirical approach. With an assumed dust density distribution, the static radiative transfer equation was solved, subject to the radiative equilibrium constraint. The resultant fluxes and specific intensities would be compared to spectral and spatial observations. Independently, a chosen velocity field and mass-loss-rate yielded, via the stationary continuity equation, a gas density distribution. It was found that fitting the observed infrared line profiles required a flow velocity field having a number of acceleration regions. The suggestion was that such a velocity field might result from successive formation of different dust grain species at different temperatures. More complicated situations could be imagined, e.g. distinct shells, multiple shocks etc. However, without an ab-initio (and much more internally consistent) simulation, the number of adjustable parameters is unreasonably large, making the semi-empirical approach too arbitrary.

On the other hand, hydrodynamic models have been developed to investigate the mass loss mechanism of these pulsating stars. It was found, that the pulsation of the star alone cannot account for the generation of a wind exhibiting the observed mass loss rates and outflow velocities. Therefore, Wood (1979) introduced an additional term into the equation of motion (in form of a parameterized step function) in order to account for radiation pressure on dust. The resulting models in fact were able to reproduce the observed mass loss rates and terminal outflow velocities. While Wood (1979) considered the limiting cases of adiabatic shocks and isothermal shocks, respectively, Bowen (1988) extended this kind of model calculations by introducing parameterized cooling laws to treat the relaxation of the gas after the passage of a shock. In these models, a thermally driven wind is generated by a 'calorisphere' which results from the rather inefficient cooling laws used by Bowen (1988). Also in these models, the mass loss rate is strongly enhanced by introducing a temperature sensitive parameterized step-function to account for radiation pressure on dust. The first time-dependent models which considered in detail the formation of dust and its interaction with the hydrodynamic and thermodynamic structure of the wind have been presented by Fleischer et al. (1991, 1992) and, using a different numerical scheme for the solution of the equation system, by Feuchtinger et al. (1993). These models revealed, that a proper treatment of the dust formation problem is essential to disclose the dominant role of the dust not only for the local hydrodynamic and thermodynamic conditions but also for the temporal behavior of the wind (e.g. Winters et al. 1994b, Fleischer et al. 1995, Höfner et al. 1995).

This consistent modeling approach already has been successfully applied to the extreme carbon star AFGL 3068 by Winters et al. (1997), reproducing the observed outflow velocity, spectral energy distribution at different phases, and the light curves of this object. In the present paper we investigate infrared CO molecular line profiles as they result from from this kind of model calculations.

In Sect. 2 we summarize how our dynamical models of circumstellar dust shells around LPVs are calculated and describe the method adopted here for the molecular line calculations. Our general results are presented in Sect. 3. In particular, we discuss the dependence of the synthetic line profiles on the the model parameters and analyze their temporal evolution. Following these theoretical considerations, in Sect. 4.1 a short description of high resolution infrared CO line observations of IRC +10216 is given and the theoretical results are compared with the observed CO line profiles in Sects. 4.2 and 4.3 for specific model calculations. We finish this paper in Sect. 5 with a summary of the results obtained from the present models.

2. Modeling method

2.1. Time–dependent hydrodynamical model calculation

Our approach to model circumstellar dust shells around LPVs is described in detail in Fleischer et al. (1992) and Winters et al. (1997). It comprises

- the explicit solution of the time dependent hydro–equations in Lagrangian coordinates for a spherical symmetric geometry according to the scheme of Richtmyer & Morton (1967),
- a detailed treatment of the formation, growth and evaporation of carbon grains by means of the moment method (Gail & Sedlmayr 1988, Gauger et al. 1990), which includes an equilibrium chemistry for the important hydrocarbons,
- the treatment of continuum radiative transfer in terms of frequency integrated moments by a generalized Eddington approximation for a spherical grey atmosphere (see Unno & Kondo (1976) and Hashimoto (1995) for details),
- the description of post-shock cooling of the gas by an LTE cooling function
- the simulation of the interior pulsation by a sinusoidally moving inner boundary (piston).

These models are determined by the four stellar parameters: present mass M_*, luminosity of the initial model $L_*(t=0) = L_0$, effective temperature of the initial model $T_*(t=0) = T_0$, and the element abundances ϵ_i (especially the carbon abundance ϵ_C, all other elements are assumed to have solar abundance), and by the pulsation period P and velocity amplitude Δv_p of the piston motion. The stellar radius of the initial model $R_*(t = 0) = R_0$ follows from L_0 and T_0 by means of the Stefan-Boltzman law.

The calculations start from an initially dust free hydrostatic model. Then, the time evolution is followed until a cyclic or 'regular' pattern develops.

2.2. Molecular line calculations

The synthetic infrared CO line profiles for the fundamental (v 0-1) and first overtone (v 0-2) lines are calculated using the

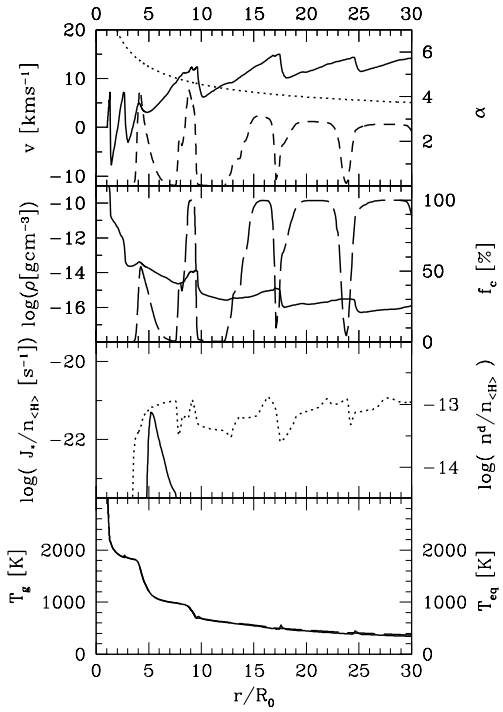

Fig. 1. Radial structure of Model W64 at t = 77.25 P *Upper panel:* velocity v (solid line), escape velocity (dotted line) and radiative acceleration on dust normalized to the local gravitational deceleration α (dashed line) *Second panel:* density (solid) and degree of condensation $f_{\rm c}$, i.e. fraction of C–atoms not bound in CO, which are actually condensed into grains (dashed) *Third panel:* grain formation rate $J_*/n_{\langle \rm H \rangle}$ (solid line) and number of grains per H–atom $n^{\rm d}/n_{\langle \rm H \rangle}$ (dotted) *Lower panel:* gas temperature $T_{\rm g}$ (solid) and radiative equilibrium temperature $T_{\rm eq}$ (dashed) (virtually equal, due to the assumed effective coupling between gas and radiation)

radial structure for the velocity, density, and temperature of the gas and the dust, which result at a given instant of time from the dynamical model calculations described in the previous section.

The original procedure used in Keady (1982) and Keady et al. (1988) involved solving coupled statistical equilibrium equations (allowing for vibrational non-LTE) and comoving frame transport equations to determine the vibrational populations and source functions. These were subsequently used in a formal solution of the observer's frame radiation transport equation to synthesize the flux profiles. These non-LTE calculations indicated that the CO vibrational level populations are essentially in equilibrium at the dust temperature for optically thick dust shells.

Therefore, in the present calculations the vibrational level populations are determined from a Boltzmann distribution at the dust temperature, and are used in the solution of the observer's frame transport equation.

Finally, all of the calculated line profiles have been Fourier smoothed to the instrumental resolution of the Fourier transform spectrometer for easy comparison with the observations.

It would be interesting to verify that the vibrational level populations are in equilibrium at the dust temperature for the present more realistic (and complicated) spatial distributions. However, the original procedure cannot be applied here, because the comoving frame solution utilized the Rybicki variation of the Feautrier scheme, which is valid for monotonic velocity fields only.

3. Results

3.1. Dust shell structure

The parameter and some resultant quantities of the dust shell models discussed in this paper are given in Table 1. The models were chosen to cover a broad range in mass loss rates but to have similar outflow velocities of the order of $15\,\mathrm{km\,s^{-1}}$. Model W70 (see Table 1) results in a somewhat higher outflow velocity than that and a significantly higher dust-to-gas ratio than the other models. Both properties are essentially caused by the higher C/O ratio adopted for this model. The general dependence of the resultant quantities on the model parameters is discussed in Arndt et al. (1997).

Since the radial structure of the dynamical dust shell models is qualitatively similar, we show only the structure of Model W64 as an example in Fig. 1 for one instant during the pulsation cycle ($t = 0\,\mathrm{P}$ refers to the hydrostatic initial model).

The process of dust formation depends sensitively on the local temperature and density, which vary substantially in the inner parts of the atmosphere due to the passage of shocks generated by the interior pulsation. Therefore, grains can form only in a limited radius interval and during certain phases of the cycle. On the other hand the grains themselves decisively affect the hydro– and thermodynamic structure of the flow. This interaction leads to a variety of dust induced dynamical phenomena (Fleischer et al. 1991, 1992):

1. Inhomogeneous layered distribution of the circumstellar dust caused by the variation of temperature, density, and chemical composition in the dust forming region (cf. the stratification of the degree of condensation $f_{\rm c}$ and the radiative acceleration α in Fig. 1).
2. Strong shocks dominating the shell structure, either generated by pulsation and amplified by radiation pressure on grains, or even produced by the radiation pressure alone (cf. the velocity field in Fig. 1).
3. Substantial back-warming of the atmosphere inside the dust layers due to the dust opacity, where in turn the temperature increase terminates condensation (cf. the temperature stratification and the sharp cut-off of the nucleation rate at its "inner" edge in Fig. 1).

In this model a new dust layer is formed only once in about four pulsation cycles, which implies a repetition of the radial pattern of the CDS on the same time scale. Fleischer et al. (1995) showed, that the dust formation process in the circumstellar shell is controlled by a time scale of its own, which generally differs from the time scale of the interior pulsation. This time scale is decisively determined by the abundance of the dust–forming elements, i.e. by the carbon abundance $\epsilon_{\rm C}$ for the models discussed here. Depending on its value, the spatial structure of the

Table 1. Parameters and time-averaged resultant quantities of five models

Model	M_*	L_0	T_0	$\epsilon_{\rm C}/\epsilon_{\rm O}$	P	Δu_p	R_0	$\left\langle \dot{M} \right\rangle$	$\langle v_\infty \rangle$	$\left\langle \rho^d/\rho^g \right\rangle$
	$[M_\odot]$	$[10^4 L_\odot]$	[K]		[d]	[km s^{-1}]	[10^{13} cm]	$10^{-5} M_\odot$yr^{-1}	[km s^{-1}]	[10^{-3}]
W70	0.8	0.75	3000	1.50	640	2	2.2	0.2	19.1	2.2
W43	0.8	0.8	3000	1.35	650	6	2.3	1.6	16.0	1.4
IRC34	0.8	0.8	3000	1.30	650	8	2.3	2.2	13.5	1.2
W64	1.0	1.0	2600	1.30	640	5	3.4	4.3	12.6	1.2
W34	0.8	1.5	2200	1.30	650	2	5.9	14.2	15.8	1.4

models repeat after one pulsation period, or after multiples of the period (*multi-periodicity*), or it even does not repeat at all. In the latter case dust formation still takes place in regular intervals, but the local conditions and thus the condensation efficiency are different, resulting in an irregular pattern of the shell.

The spatial structure of the dust shell models and its time variation manifest themselves in the infrared appearance of the models. The calculated brightness profiles show a time variable step–like structure on a scale of a few stellar radii, corresponding to the discrete shell–like distribution of the dust (Winters et al. 1995). The synthetic infrared light curves follow the periodic variation of the luminosity with superimposed shifts of the mean magnitude and changes of the amplitude, which reflect the long–term variations of the spatial structure of the outflow (Winters et al. (1994b, 1997) and Winters et al. (1999), where the light curves of Model W64 are shown). Similar behavior has been reported for observed light curves of actual objects (e.g. Le Bertre 1992).

A characteristic feature of our models is the step-like temperature distribution in the inner region of the atmosphere, produced by back-warming from the dust layers. The innermost plateau in the temperature profile is generally situated in the region $2R_0 \lesssim r \lesssim 4R_0$, inside of the dust formation zone (see e.g., Fig. 1). The temperature in this region is around 1800 K and the mass density is of the order of a few 10^{-14}g cm^{-3}, which translates to a total hydrogen number density $n_{\langle \rm H \rangle}$ of a few 10^{10}cm^{-3}. During a dust formation cycle (~ 4 P for the model shown in Fig. 1), the temperature in this region varies by less than 300 K (see also Fig. 7). These characteristic values are in reasonable agreement with the properties of the "radio photospheres" detected by Reid & Menten (1997) in six oxygen-rich long-period variable stars.

3.2. Synthetic CO infrared line profiles

3.2.1. Dependence of the line profiles on the mass loss rate and the dust optical depth of the models

Figs. 2-6 show radial shell structures and the corresponding synthetic CO (v 0-1) fundamental band (at $\lambda \approx 4.6\,\mu$m) and CO (v 0-2) first overtone line profiles (at $\lambda \approx 2.3\,\mu$m) in velocity space at fixed instants of time for the five models given in Table 1, ordered in a sequence of increasing mass loss rate. Positive velocities indicate out-flowing material, negative velocities indicate motions towards the star.

In all models considered here, the fundamental band lines show a pronounced P-Cygni emission component and the line cores are completely saturated. In contrast, the first overtone transitions are much less saturated due to their lower oscillator strength, and little P-Cygni emission is expected as after an excitation from $v = 0$ to $v = 2$ the subsequent decay to $v = 1$ is more likely than to the $v = 0$ state.

Model W70 yields the lowest mass loss rate of $\dot{M} = 2\,10^{-6} M_\odot$yr^{-1} in the sequence considered here and an average dust-to-gas ratio of $\rho^{\rm d}/\rho^{\rm g} = 2.2\,10^{-3}$. The dust optical depth at $4.6\,\mu$m is $\tau^{\rm d}_{4.6\,\mu} = 0.28$ at the instant of time shown in Fig. 2. Due to this rather small dust optical depth, the P-Cygni emission component in the fundamental band is rather high, it is about a factor of 4 above the continuum, and a separation between the different rotational lines is apparent (the R(1) line showing the weakest and the R(6) line the strongest emission, respectively).

The overtone lines show a clear separate three-component structure with absorption features at -8 km s^{-1}, $+7$ km s^{-1}, and $+19$ km s^{-1} respectively. These separate features are a result of the shocked atmospheric structure. The line depth of the absorption component at $+19$ km s^{-1} depends on rotational excitation, it is $\approx 60\%$ of the continuum level for the R(10) line, whereas the R(25) line reaches 80% of the continuum level. This absorption feature indicates material moving at the final outflow velocity, whereas both low velocity features emerge from the inner region of the shell and are indicative for the material associated with the innermost, purely pulsation-generated shock (feature at -8 km s^{-1}) and for the material moving just in front of the first dust accelerated shock (absorption at $+7$ km s^{-1}), respectively.

Fig. 3 depicts the radial structure and the line profiles emerging from Model W43 which has an average mass loss rate about a factor of 8 higher than Model W70 whereas the dust-to-gas ratio is a factor 1.6 smaller. This leads to a dust optical depth for the instant of time shown in Fig. 3 of $\tau^{\rm d}_{4.6\,\mu} = 1.64$. Due to the higher dust optical depth, the resulting P-Cygni emission component in the fundamental band is about a factor of 2.2 weaker than in Model W70, it is 76% above the continuum (note the different scaling of the ordinate in the plot of the fundamental band line). No separation occurs between the R(1), R(3) and R(6) profiles.

The overtone lines are not saturated at the mass loss rate of $1.6\,10^{-5} M_\odot$yr^{-1} (the R(10) line core is at 10% of the continuum level) and show a component structure of the main absorption trough with features at $+2$ km s^{-1}, $+11$ km s^{-1}, and

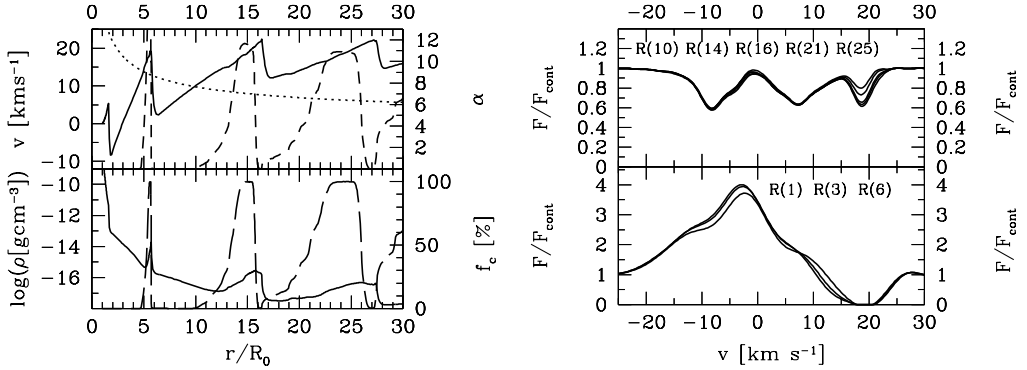

Fig. 2. Radial shell structure (l.h.s.): velocity (solid), escape velocity (dotted), and radiative acceleration α (dashed) (upper diagram) and mass density ρ (solid) and degree of condensation f_c (dashed) (lower diagram). Calculated (v 0-1) fundamental band lines (r.h.s., lower diagram) and (v 0-2) overtone lines (r.h.s., upper diagram) for Model W70

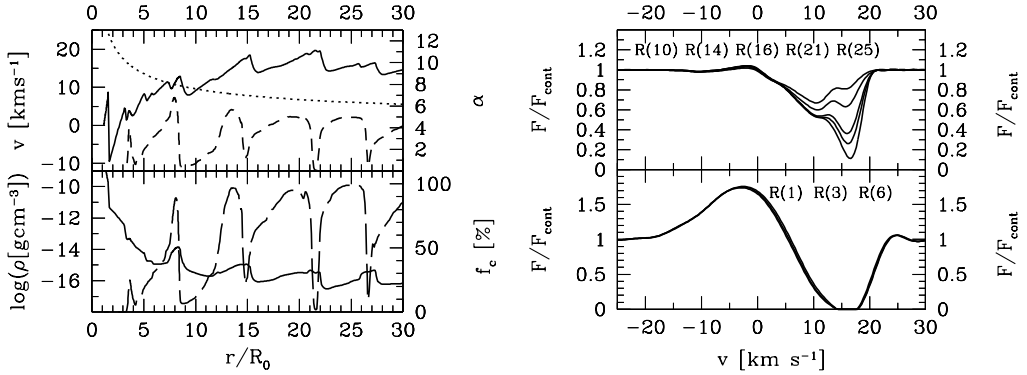

Fig. 3. Same as Fig. 2 for Model W43

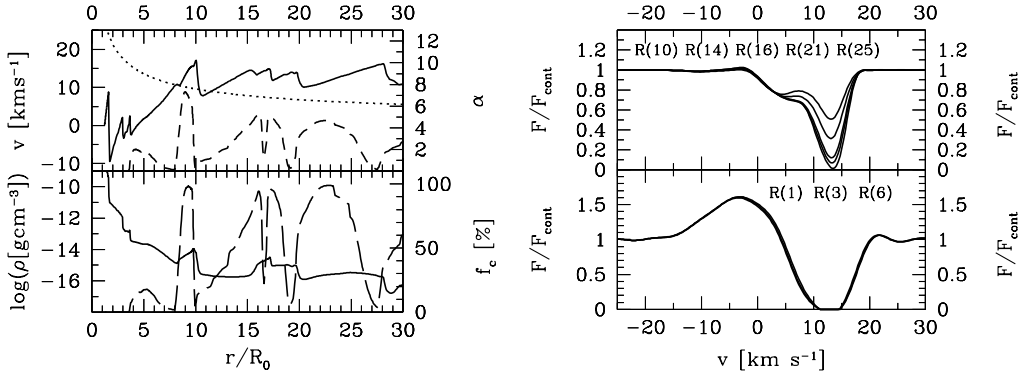

Fig. 4. Same as Fig. 2 for Model IRC34

$+16\,\mathrm{km\,s^{-1}}$ respectively, for the instant shown in Fig. 3. The in-falling material, associated with the innermost, purely pulsation generated shock is barely reflected (shallow dip around $-10\,\mathrm{km\,s^{-1}}$) in the line profiles (this shock is located at an continuum optical depth of $\tau_{2.3\,\mu} = 4.8$). There is a small shift of the position of the $+16\,\mathrm{km\,s^{-1}}$ absorption core with rotational excitation. Starting with the R(21) line, the $+11\,\mathrm{km\,s^{-1}}$ absorption associated with the dust layer at $7R_0$ becomes stronger than the $+16\,\mathrm{km\,s^{-1}}$ feature (probing the material outside of $15R_0$).

Model IRC34 has an time-averaged mass loss rate of $2.2\,10^{-5} M_\odot \mathrm{yr}^{-1}$ and a dust-to-gas ratio of $1.2\,10^{-3}$. This results in a dust optical depth in the fundamental band for the instant shown in Fig. 4 of $\tau^{\mathrm{d}}_{4.6\,\mu} = 1.83$. Accordingly, the P-Cygni emission component in the fundamental band is further reduced, it is 61% above the continuum level.

The R(10) overtone line is already saturated at this mass loss rate and the profiles show a two-component structure with absorption features occurring at $4.5\,\mathrm{km\,s^{-1}}$ and $12.8\,\mathrm{km\,s^{-1}}$, respectively for the instant shown in Fig. 4.

The line profiles of Model W64, which has an average mass loss rate of $4.3\,10^{-5} M_\odot \mathrm{yr}^{-1}$, are shown in Fig. 5. Due to the further increased dust optical depth at $4.6\,\mu$m of $\tau^{\mathrm{d}}_{4.6\,\mu} = 3.70$,

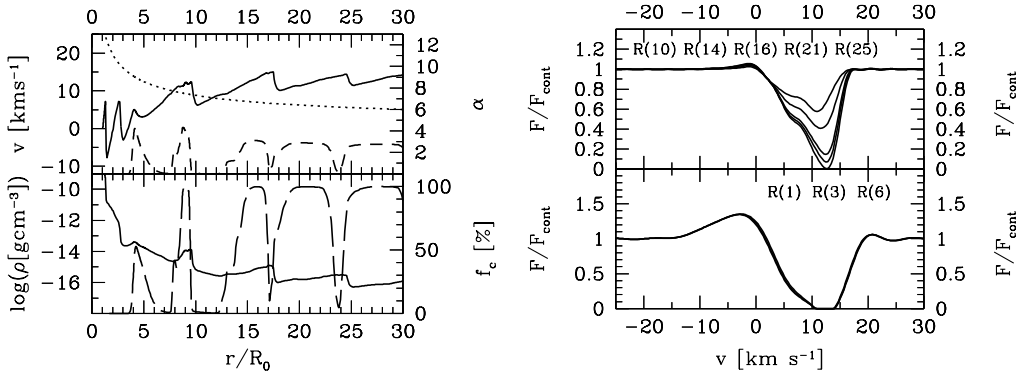

Fig. 5. Same as Fig. 2 for Model W64

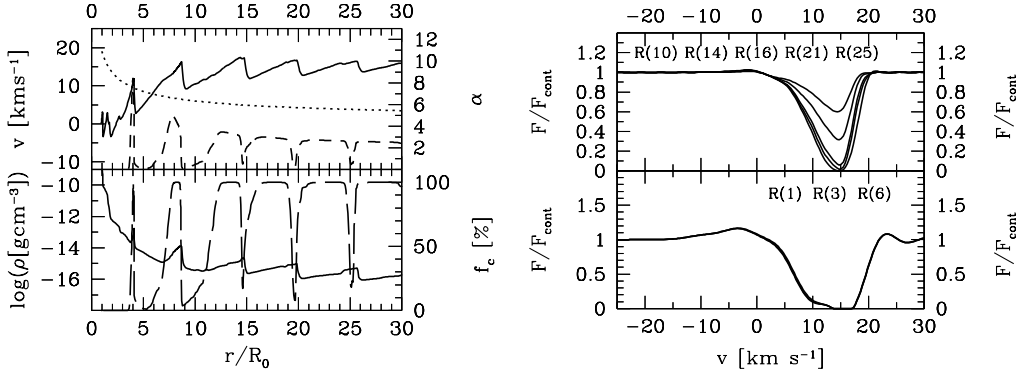

Fig. 6. Same as Fig. 2 for Model W34

the P-Cygni emission component in the fundamental band is reduced to about 35% above the continuum level.

The overtone lines are saturated up to the R(10) line (the R(14) line core is at 7% of the continuum) and again show a component structure with absorption features at $5\,\mathrm{km\,s^{-1}}$ and $12.5\,\mathrm{km\,s^{-1}}$ respectively, for the instant shown in Fig. 5. At that instant, there is a shift of the position of the main absorption core with rotational excitation by about $2\,\mathrm{km\,s^{-1}}$, the R(25) absorption core is located at $10.9\,\mathrm{km\,s^{-1}}$. The $5\,\mathrm{km\,s^{-1}}$ absorption component probes the material moving with the newly forming dust layer around $5R_0$ (see the radial structure of this model in the l.h.s. diagram).

Model W34 has the highest mass loss rate of our sample, $\dot{M} = 1.4 \cdot 10^{-4} M_\odot \mathrm{yr}^{-1}$. Together with the dust-to-gas mass ratio of $1.4 \cdot 10^{-3}$ the dust optical depth at $4.6\,\mu$m becomes rather high, at the instant shown in Fig. 6 $\tau^{\mathrm{d}}_{4.6\mu} = 6.51$, leading to a further suppression of the P-Cygni emission component to a value of 16.6% above the continuum. The fundamental band absorption is very broad, showing a secondary feature at $10\,\mathrm{km\,s^{-1}}$ produced by the material moving in front of the second dust layer located at $\approx 9R_0$.

The overtone lines are saturated up to R(10) and show practically no internal structure. There is also no shift of the position of the $14.4\,\mathrm{km\,s^{-1}}$ absorption core with rotational excitation.

The most useful diagnostic information from the fundamental lines is the strength of the P-Cygni emission component which depends on the dust optical depth. Since the absorption core is already saturated at a mass loss rate of $\approx 2\,10^{-6} M_\odot \mathrm{yr}^{-1}$, the fundamental lines cannot be used to derive mass loss rates even in this range of relatively small values. In contrast, the first overtone lines clearly reflect the shocked, layered structure of the inner shell region by showing a pronounced multi-component structure. At least the lines of higher rotational excitation ($J_l > 10$) are not saturated even for mass loss rates of the order of $10^{-5} M_\odot \mathrm{yr}^{-1}$ and thus can be used to constrain the mass loss rate.

3.2.2. Temporal variation of the CO first overtone lines

Whereas the fundamental band lines mainly reflect the conditions in the outer regions of the CDS where the dust formation process is already completed, the first overtone lines are sensitive to the inner, dust formation region. Since the formation of new dust layers takes place on time scales longer than the pulsation period, the respective temporal changes of the physical conditions should result in corresponding long term temporal variations of the line profiles. In the models presented here, a dust layer is formed every 2 pulsation periods in Model W70, approximately every 3 periods in Model W43, every ≈4 periods in Models W64 and W34, respectively and approximately every 6 pulsation periods in Model IRC34.

To illustrate the temporal changes of the overtone line profiles caused by the dynamical behavior of the models, Fig. 7 shows a time sequence of the shell structure (l.h.s. diagrams: ve-

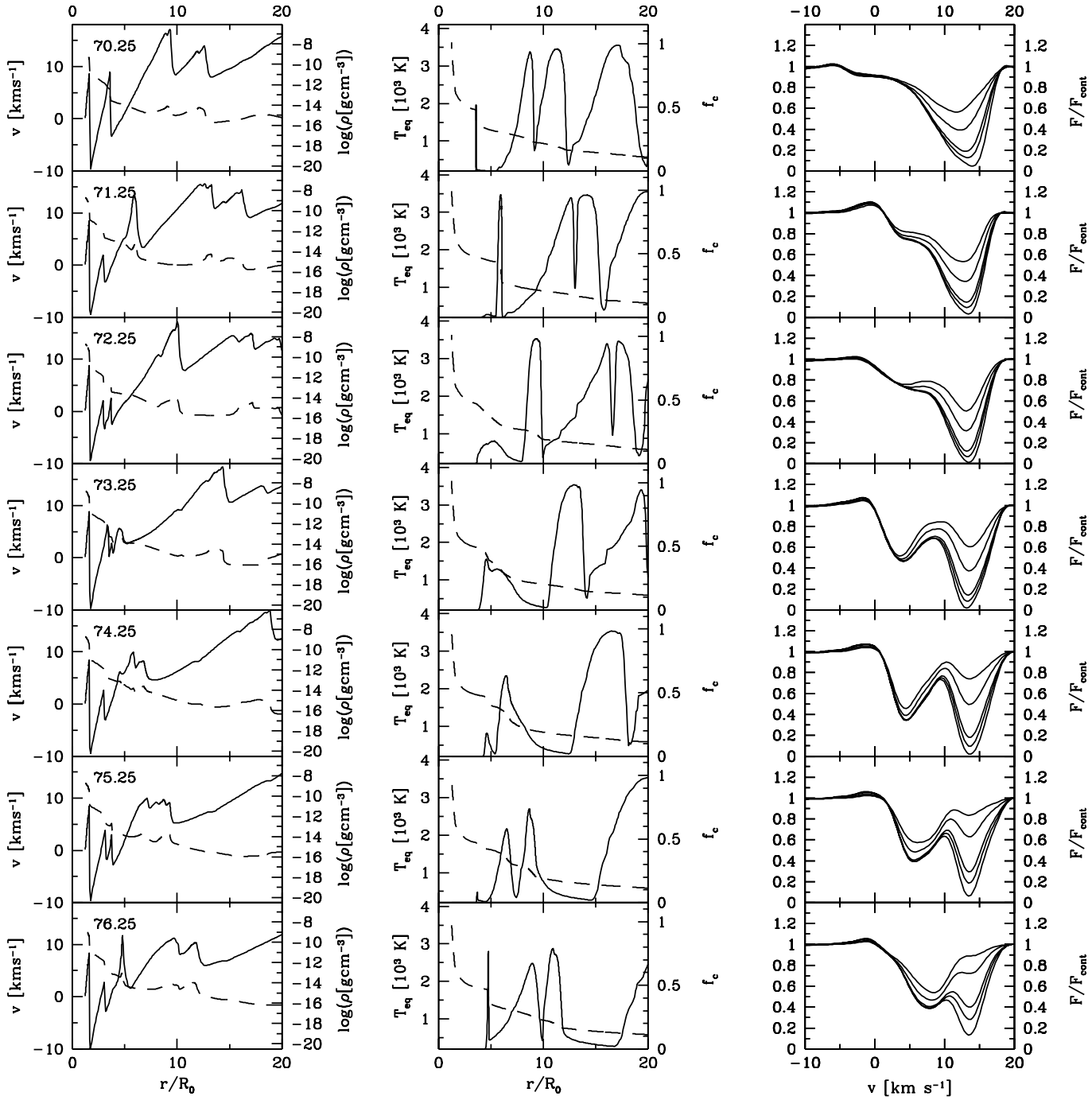

Fig. 7. Radial shell structure (l.h.s. and middle column) and corresponding first overtone line profiles (R(10), R(14), R(16), R(21), and R(25) in order of decreasing strength) (r.h.s) for Model IRC34 at 7 different instants of time, separated by one pulsation period each

locity (solid line) and density (dashed line), middle diagrams: degree of condensation (solid line) and temperature (dashed line)) and of the corresponding synthetic first overtone line profiles (r.h.s. diagrams) of Model IRC34. The instants shown in Fig. 7 are separated by one pulsation cycle each. One clearly sees, that the radial structure and also the shape of the line profiles do not repeat from cycle to cycle.

This model produces alternating single– and double-peaked dust layers as can be seen from the radial distribution of the degree of condensation (compare the instants $t = 70.25\,\mathrm{P}$, $t = 73.25\,\mathrm{P}$, and $t = 75.25\,\mathrm{P}$). These dust layers are accelerated and driven outwards by radiation pressure (see e.g. the sequence $t = 70.25\,\mathrm{P} \ldots t = 74.25\,\mathrm{P}$). The radial structure of the shell (i.e. the position of the dust layers) approximately repeats after 6 cycles in this model (compare $t = 70.25\,\mathrm{P}$ and $t = 76.25\,\mathrm{P}$), but since the degree of condensation and, consequently the radiation force, is lower for the later instant, the corresponding layers are moving at different velocities, being

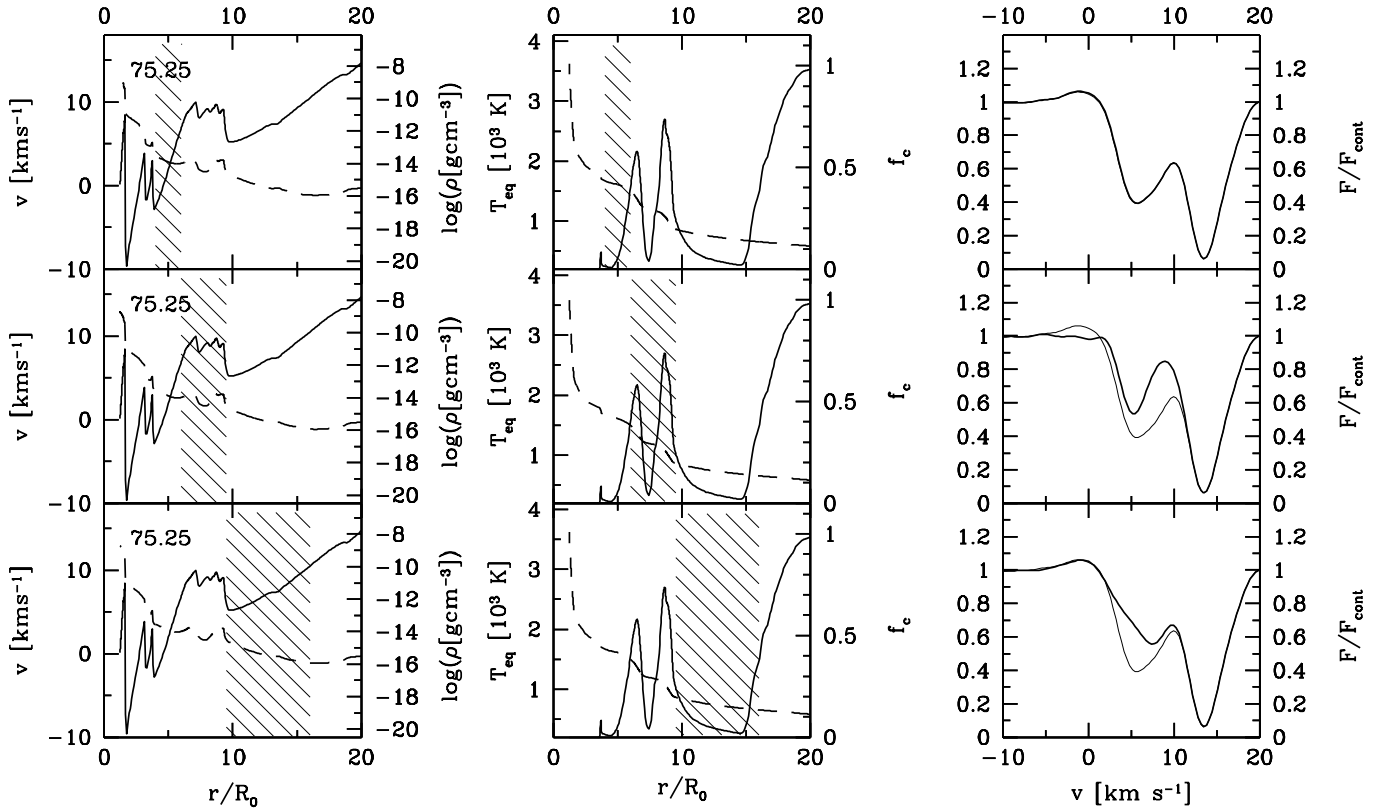

Fig. 8. Radial shell structure (l.h.s. and middle column) and corresponding first overtone R(10) line profile (r.h.s) for Model IRC34 at $t = 75.25$ P, where CO absorption is suppressed in different radial zones (shaded areas)

lower at the later instant. A new double-peaked layer forms between $t = 72.25$ P and $t = 75.25$ P in the region around $5R_0$ (e.g. middle diagram, f_c) which, by momentum coupling accelerates the gas and leads to the formation of a new double-peaked shock. Due to back-warming by the newly formed grains, the temperature increases behind this newly forming dust layer and stays almost constant in the region between the dust layer and $r \approx 2R_0$. Additionally, the newly formed shock sweeps up the gas, producing the pronounced double-peaked density structure associated with this shock (cf. l.h.s. diagram).

The line profiles (r.h.s diagrams in Fig. 7) reflect the formation of this new layer by the evolution of a strong secondary absorption feature. The core position of this feature shifts from $v = 4\,\mathrm{km\,s^{-1}}$ at $t = 73.25$ P to $v = 8\,\mathrm{km\,s^{-1}}$ at $t = 76.25$ P while the strength of the feature increases considerably during this time interval.

3.2.3. Profile analysis at one instant of time

Since the velocity field resulting from the models is strongly non-monotonic, absorption from different spatial regions can contribute to the formation of the line profiles at a given velocity. In order to analyze the radial information contained in the profile, we have artificially suppressed CO line absorption in different radial regions of the inner part of the circumstellar shell. Fig. 8 shows the results for Model IRC34 at $t = 75.25$ P.

In the calculations shown in Fig. 8, absorption has been suppressed in different radial regions which are shaded in the corresponding radial plots. The resulting (artificial) profiles are shown in the r.h.s. column of Fig. 8 together with the 'complete' profile, indicated by the thin line. From the region just behind the innermost, dust accelerated shock located around $4 - 6R_0$, there is no contribution to the line profile, thick and thin line coincide (upper panel of Fig. 8). The material moving with the high velocity region of the double-peaked shock mainly contributes to the 'high velocity' wing of the secondary $5\,\mathrm{km\,s^{-1}}$ absorption feature and also provides the small emission component to the P-Cygni profile ($2^{\mathrm{nd.}}$ panel). Material located just in front of this shock structure is responsible for the 'low-velocity' wing of the secondary absorption feature ($3^{\mathrm{rd.}}$ panel). Thus, the secondary feature in fact probes the physical conditions and the dynamical behavior of the material associated with the innermost, dust induced shock and, therefore, is indicative for the formation of a new dust layer in the model.

Summarizing this section, we find that

- the shocked, layered structure of the shell models is clearly reflected by a multi-component structure of the corresponding first overtone CO line profiles
- the secondary (low velocity) absorption component is indicative for the dust formation region, while the main absorption component is largely produced by the material lo-

cated farther out in the shell, where the dust formation process is already completed
– the dynamics of the dust formation process is clearly reflected in the temporal evolution of the synthetic CO first overtone line profiles resulting from the models.

4. Application to IRC +10216

Since its discovery in the 1960's, IRC +10216 has been an exceptional target of numerous observational and theoretical investigations, which revealed a wealth of very detailed information about this object. However, even now its distance from earth, its luminosity, and its mass loss rate are not known too precisely. Recent investigations favor a distance of $110\,\mathrm{pc} \lesssim d \lesssim 150\,\mathrm{pc}$ (e.g., Zuckerman et al. 1986, Jura & Kleinmann 1989, Groenewegen et al. 1998) instead of $d = 270$ pc first derived by Herbig & Zappala (1970). The models discussed in the present paper have luminosities in the range $7500\,L_\odot \leq L_* \leq 15000\,L_\odot$ (see Table 1) which, assuming a total flux of $2{\cdot}10^{-12}$ W cm^2 received from IRC +10216 at earth (e.g., Ridgway & Keady 1988) would correspond to a range in distance of $110 \leq d \leq 150$ pc, much in agreement with the above values.

From previous modeling, there are indications that the mass loss rate of IRC +10216 might have changed considerably within the last $\sim$ 5000 years, being lower presently by up to a factor of 5 (e.g., Sahai 1987, Truong-Bach et al. 1991, Keady & Ridgway 1993, Groenewegen et al. 1998). If that is true, mass loss rate determinations sensitive to the outer region ($\gtrsim 50''$) of the IRC +10216 shell should result in higher values of $\dot{M}$ than do methods which probe the inner parts of the shell. Table 2 summarizes some values given for the mass loss rate and the distance in the literature. Since many mass loss rate determinations can be scaled by the distance to the object (e.g., $\dot{M} \propto d^2$ when $\dot{M}$ is derived from CO rotational lines while $\dot{M} \propto d$ for determinations from IR photometry) we also give respective values for $\dot{M}$ scaled to a distance of 135 pc to facilitate the comparison. However, such scaling can not be applied to the more sophisticated models, where the mass loss rate results from a consistent description of the circumstellar shell. In particular, a simple scaling is impossible for the models presented in this paper. E.g., increasing the luminosity of our model (thus the distance to the object), would increase the mass loss rate but at the same time it would also increase the outflow velocity of the wind and would decrease the dust-to-gas ratio and, therefore, would considerably change the synthetic line profiles (see Sect. 3.2.1). From Table 2 it seems likely, that the present day mass loss rate of IRC +10216 is close to $1 \cdot 10^{-5} M_\odot \mathrm{yr}^{-1}$. However, we note that there are two recent investigations (Crosas & Menten 1997, Skinner et al. 1999) which result in considerably (a factor of 3) higher values than this.

The most widely used mass loss rate determinations have been done from CO rotational lines, which probe the material outside of $\approx 100\,R_*$ from the star. At these distances the IRC +10216 circumstellar shell exhibits a rather spherically symmetric appearance (e.g., Mauron & Huggins 1999). However, in its inner parts where the CO infrared lines emerge, the morphology of IRC +10216 is quite different, showing a pronounced clumpyness (e.g., Weigelt et al. 1998, Haniff & Buscher 1998, Osterbart et al. 2000) and even signs of a bipolar structure (Skinner et al. 1998, Osterbart et al. 2000), suggesting that IRC +10216 might presently be transforming into a proto-planetary nebula. The application of spherically symmetric models to the inner region of IRC +10216 therefore should be taken with care. The intention of the discussion in the following sections is to demonstrate, that our time-dependent modeling approach, which is based on first principles, results in shapes of the CO infrared line profiles and of their temporal variation, which are in excellent agreement with high spectral resolution observations. However, we do not intend a rigorous quantitative modelling of IRC +10216 here.

Table 2. Gas mass loss rates and distances derived for IRC +10216 in different investigations. The last column gives the mass loss rate scaled to a distance of 135 pc and the scaling law used. o/i indicates mass loss rates derived for the outer/inner shell region

$\dot{M}$ $[10^{-5} M_\odot \mathrm{yr}^{-1}]$	d [pc]	ref.	$\dot{M}$@135 pc $[10^{-5} M_\odot \mathrm{yr}^{-1}]$	
5.7o	290	J83	1.8	$d^{3/2}$
4.4o	260	KM85	1.2	d^2
4.8o	300	S87	2.4	d
3.2i	300	S87	**1.6**	d
2.0i	200	KHR88	**0.9-1.35**	d-d^2
4.0o	200	TMN91	2.7	d
2.5i	200	TMN91	**1.1-1.7**	d-d^2
2.0o	150	K92	1.8-2	$< d$
3.25	150	CM97	2.9	d
1.16i	135	LB97	**1.16**	-
7.5o	135	GVM98	7.5	-
1.5i	135	GVM98	**1.5**	-
5.0	170	SJT99	3.9-3.2	d-d^2
$\sim$ **1**	115	present work		

References: J83 Jura (1983), KM85 Knapp & Morris (1985), S87 Sahai (1987), KHR88 Keady et al. (1988), TMN91 Truong-Bach et al. (1991), K92 Kastner (1992), CM97 Crosas & Menten (1997), LB97 Le Bertre (1997), GVM98 Groenewegen et al. (1998), SJT99 Skinner et al. (1999)

4.1. Observed CO infrared line profiles

CO infrared absorption lines emerge from the inner parts of the wind, where the flow starts and accelerates. Therefore high resolution IR spectroscopy, which resolves individual vibration rotation lines, can reveal considerable details about the dynamics in this region as has already been demonstrated by many authors (e.g. Hinkle 1978; Hinkle et al. 1982, 1984; Keady et al. 1988; Keady & Ridgway 1993). The observations of the CO fundamental and overtone lines presented in this section were obtained on various dates at the KPNO Mayall 4 meter telescope using the Fourier Transform spectrometer at the coudé focus. The integration times vary from 2 – 3 hours for the $4.6\,\mu m$ fundamental lines to 10 hours for the $2.3\,\mu m$ overtone lines. The

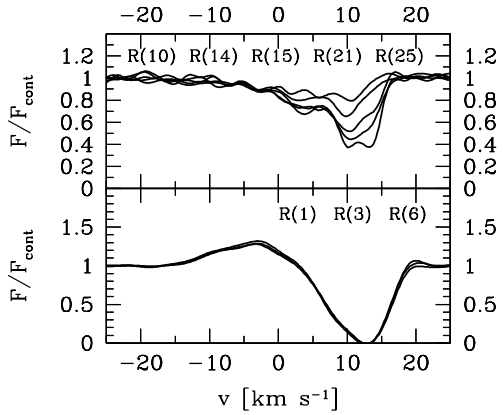

Fig. 9. Observed CO infrared line spectra of IRC +10216 obtained on Nov 6, 1981: lower diagram: fundamental (v 0-1) transitions, upper diagram: first overtone (v 0-2) transitions. Blue-shifted lines are at positive velocities.

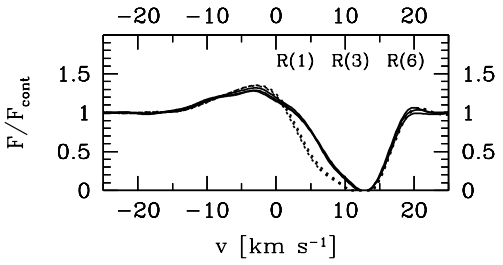

Fig. 10. Comparison of calculated (dotted) and observed (solid) fundamental lines (v 0-1) for Model W64

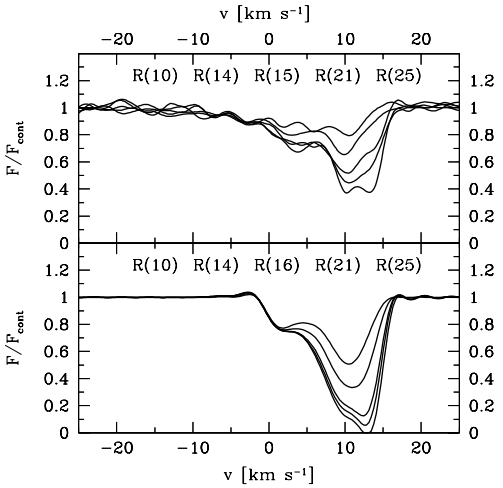

Fig. 11. Comparison of calculated (lower panel, Model W64) and observed (upper panel) (v 0-2) first overtone lines

resolution ranges from 2 – 4 km s^{-1}, and the ratios of peak signal to rms noise are typically in excess of several hundred to one.

In Fig. 9 we show observed CO line spectra of (v 0-1) fundamental band lines and (v 0-2) first overtone band lines from IRC +10216. The fundamental band lines show the classic P-Cygni profiles with an emission component of $\approx 30\%$ above the continuum and an extremely saturated blue-shifted absorption core at $\approx 14\,\mathrm{km\,s^{-1}}$. Owing to the tremendous saturation the most useful information is provided by the P-Cygni emission component, which constrains the dust optical depth in the $5\,\mu\mathrm{m}$ region to values between about $2-4$, as otherwise either too much (for smaller dust optical depth) or too little emission (for larger optical depth) would result (see Sect. 3.2.1). The observed overtone lines show a multi–component absorption structure extending out to $14\,\mathrm{km\,s^{-1}}$, and the location and strength of the individual absorption components (e.g. at $10\,\mathrm{km\,s^{-1}}$) depends on the rotational excitation. These properties make them suitable to probe the velocity field in the acceleration region of the wind.

4.2. Comparison of the synthetic CO lines with the observations

The synthetic infrared CO line profiles of Model W64 are shown in Figs. 10 and 11 together with the corresponding observed profiles.

Fig. 10 shows a direct comparison of the calculated fundamental band lines with the corresponding observations of IRC +10216. The agreement of the blue wing of the absorption profile is almost perfect and also the P-Cygni emission component agrees rather well. There is however a noticeable discrepancy in the red wing of the absorption component, indicating that the model provides too much absorption (and, thus, too much CO) at low expansion velocities.

The calculated (v 0-2) overtone lines (Fig. 11) show the effect of the high CO density in the model much more dramatically. The calculated overtone lines show a multi-component structure very similar to the observations (cf. Fig. 11). This self-consistent dynamical model qualitatively reproduces the observed velocity shifts seen with increasing rotational excitation. However, the calculated lines are much too strong compared to the lines from IRC +10216, indicating that the CO density and, thus, possibly the mass loss rate in the model, is too high.

4.3. Modeling the temporal variation of the CO first overtone lines observed for IRC +10216

Fig. 12 shows the synthetic P(7) line profiles of the (v 0-2) transition resulting from Model IRC34 at different instants of time. The absorption extends from about zero velocity to $\approx 17\,\mathrm{km\,s^{-1}}$, and the main absorption core is located at $\approx 14\,\mathrm{km\,s^{-1}}$, showing only slight variations of its strength and exact location with time. After $t = 70.25\,\mathrm{P}$, a secondary absorption feature starts to develop at $\approx 5\,\mathrm{km\,s^{-1}}$, which considerably increases its strength during the following time interval, and simultaneously shifts to higher velocities. According to the discussion presented in Sect. 3.2.2, this feature indicates the formation of a new dust layer in the model.

The radial structure of the dust shell model was shown in Fig. 7 at $t = 72.25\,\mathrm{P}$ and $t = 73.25\,\mathrm{P}$, i.e. at two phases enclosing the development of the feature. During this time a new

dust layer is formed in the model. Radiation pressure acting on this new dust leads to the acceleration of a dust amplified shock starting at a material velocity $v < 5\,\mathrm{km\,s^{-1}}$, and to an enhanced density of the matter in the inner radial region overrun by the shock. Subsequently the velocity of the accelerated material increases further, while the temperature and density at the corresponding positions decrease due to the expansion. Thus, the secondary absorption feature at first gets stronger until it weakens again after $t = 74.25$ P.

In Fig. 13 the temporal evolution of the synthetic line profiles from Model IRC34 is compared with observed (v 0-2) P(7) overtone lines from IRC +10216. The dates of the observations are separated by ≈ 2.5 P and ≈ 3.5 P, where P $= 650$ d is the pulsation period adopted for IRC +10216. The observed spectra (l.h.s. diagrams) nicely show the development of a low–velocity absorption feature around $5\,\mathrm{km\,s^{-1}}$, and it is worth noting that this feature evolves on approximately the same time scale in the observations and the calculations (r.h.s. diagram, for the synthetic profiles the CO abundance has been reduced by a factor of 0.33 in order to match the observed line strengths).

From the model calculations presented here, we would expect that the secondary feature in the CO overtone line profiles from IRC +10216 should disappear and re-appear on the dust formation time scale of about 6 pulsation periods, corresponding to ≈ 10 yr. To confirm this prediction, a continuing high resolution infrared monitoring in the $2.3\,\mu$m spectral region would be needed.

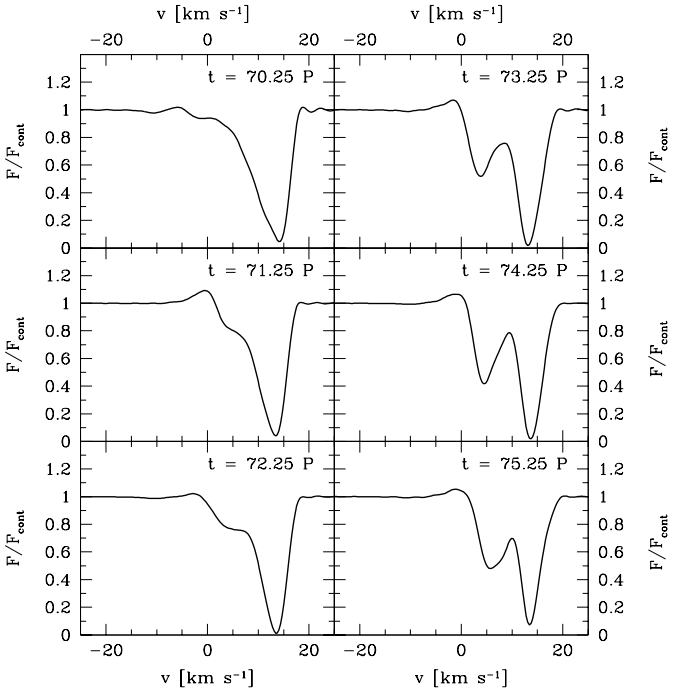

Fig. 12. Synthetic CO (v 0-2) P(7) line profiles from Model IRC34 at different instants of time

5. Concluding remarks

We have presented simplified non-LTE radiative transfer calculations for CO (v 0-1) fundamental and (v 0-2) overtone lines, using the structure of dynamical models for dust shells around carbon-rich long-period variables, which result from a consistent treatment of hydro- and thermodynamics, radiative transfer, chemistry and carbon grain formation.

Due to the saturation of the fundamental band lines already at a mass loss rate of $2\,10^{-6} M_\odot \mathrm{yr}^{-1}$ the most useful information is provided by the P-Cygni emission component, which is sensitive to the dust optical depth in the $5\,\mu$m region. In contrast, the first overtone lines clearly reflect the shocked, layered structure of the inner shell region by showing a multi-component structure. At least the line cores of higher rotational excitation ($J_l > 10$) are not saturated even for mass loss rates of the order of $10^{-5} M_\odot \mathrm{yr}^{-1}$ and thus can be used to constrain the mass loss rate. A secondary (low velocity) absorption component appearing in the overtone line profiles is indicative for the dust formation region, while the main absorption component is largely produced by the material located farther out in the shell, where the dust formation process is already completed. We have demonstrated that the dynamics of the dust formation process is in particular reflected in the temporal evolution of the synthetic CO first overtone line profiles resulting from the models.

The comparison of synthetic infrared CO line profiles calculated on the basis of dynamical dust shell models with the lines observed in IRC +10216 shows, that one model yields a

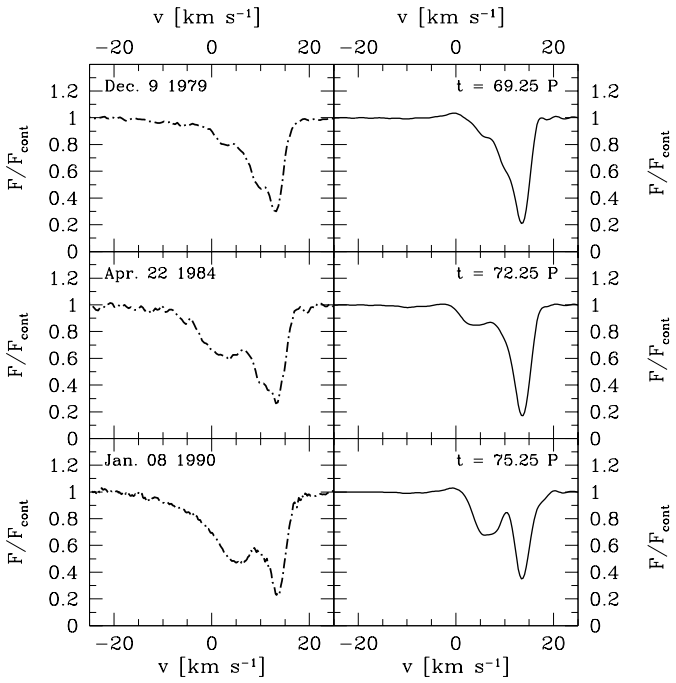

Fig. 13. Temporal variation of (v 0-2) P(7) line profiles. **l.h.s. column**: Observed line profiles from IRC +10216 (Sada 1993); **r.h.s. column**: Calculated line profiles from Model IRC34

dust distribution, which lies well within the limits set by the observations. The general shape of the calculated fundamental lines resembles the observed ones indicating, that the velocity structure of the model represents at least the general properties of the actual structure in IRC +10216. However, the differences

in the strengths of the overtone lines show, that the resulting mass loss rate of the model is about a factor of three too high, indicating that it should be closer to the value of $1\,10^{-5} M_{\odot}\mathrm{yr}^{-1}$ derived earlier, e.g. by Keady et al. (1988).

The synthetic (v 0-2) CO infrared line profiles calculated on the basis of a second dust shell model resemble the multi–component structure and the time variations of corresponding lines in the observed spectra, which thereby are interpreted as a consequence of the dynamical structure and its temporal variation in the inner parts of the wind. Especially the emergence and subsequent evolution of a secondary low–velocity absorption feature can be understood as a result of a dust formation event and the subsequent acceleration of the matter by radiation pressure on dust. However, the line strengths of the calculated profiles are again too high, indicating that the CO density and, thus, possibly the mass loss rate of the dust shell model is too large. The reason for this discrepancy might lie in our simplified description of the gas opacity in the atmospheric structure calculation, where we assume a constant value of $\kappa^{\mathrm{g}}/\rho = 2 \cdot 10^{-4}\mathrm{cm}^2\mathrm{g}^{-1}$ (cf. Bowen 1988). As has been pointed out by Höfner et al. (1998) and by Helling et al. (2000), a more realistic description of the gas opacity leads to a general reduction of the gas density and, thus, of the mass loss rate resulting from the models. Moreover, effects of the pronounced clumpy structure of the inner shell region of IRC +10216 (Weigelt et al. 1998, Haniff & Buscher 1998) have not been taken into account in our present spherically symmetric modeling approach.

Acknowledgements. We thank the referee Dr. M. Jura for useful suggestions on the manuscript. The calculations were performed on the Cray computers of the Konrad-Zuse-Zentrum für Informationstechnik Berlin and on the Crays of the Computing Division at Los Alamos National Laboratory. Subsequent data analysis has been performed on the WAP–cluster of the physics department of the TU–Berlin. This work has been supported by the BMBF (grant 05 3BT13A 6). Research at Los Alamos National Laboratory was performed under the auspices of the U.S. Department of Energy.

References

Arndt T.U., Fleischer A.J., Sedlmayr E., 1997, A&A 327, 614
Bowen G.H., 1988, ApJ 329, 299
Cherchneff I., Glassgold A.E., Mamon G.A., 1993, ApJ 410, 188
Crosas M., Menten K.M., 1997, ApJ 483, 913
Feuchtinger M.U., Dorfi E.A., Höfner S., 1993, A&A 273, 513
Fleischer A.J., Gauger A., Sedlmayr E., 1991, A&A 242, L1
Fleischer A.J., Gauger A., Sedlmayr E., 1992, A&A 266, 321
Fleischer A.J., Gauger A., Sedlmayr E., 1995, A&A 297, 543
Gail H.-P., Sedlmayr E., 1988, A&A 206, 153
Gauger A., Gail H.-P., Sedlmayr E., 1990, A&A 235, 345
Gehrz R.D., 1989, in: Allamandola L.J., Tielens A.G.G.M., Interstellar Dust. Dordrecht: Kluwer Academic Publishers, p. 445
Groenewegen M.A.T., 1997, A&A 317, 503
Groenewegen M.A.T., van der Veen W.E.C.J., Matthews H.E., 1998, A&A 338, 491
Habing H., 1996, A&AR 7, 97
Haniff C.A., Buscher D.F., 1998, A&A 334, L5
Hashimoto O., 1995, ApJ 442, 286
Helling C., Winters J.M., Sedlmayr E., 2000, A&A 358, 651
Herbig G.H., Zappala R. R., 1970, ApJ 162, L15
Hinkle K.H., 1978, ApJ 220, 210
Hinkle K.H., Hall D.N.B., Ridgway S.T., 1982, ApJ 252, 697
Hinkle K.H., Scharlach W.W.G., Hall D.N.B., 1984, ApJS 56, 1
Höfner S., Feuchtinger M.U., Dorfi E.A., 1995, A&A 297, 815
Höfner S., Jørgensen U.G., Loidl R., Aringer B., 1998, A&A 340, 497
Jura M., 1983, ApJ 275, 683
Jura M., 1994, ApJ 434, 713
Jura M., Kleinmann S.G., 1989, ApJ 341, 359
Kastner J.H., 1992, ApJ 401, 337
Keady J.J., 1982, The circumstellar envelope of IRC +10216, PhD thesis. New Mexico State: University, Las Cruces, New Mexico
Keady J.J., Ridgway S.T., 1993, ApJ 406, 199
Keady J.J., Hall D. N.B., Ridgway S.T., 1988, ApJ 326, 832
Knapp G.R., Morris M., 1985, ApJ 292, 640
Le Bertre T., 1992, A&AS 94, 377
Le Bertre T., 1997, A&A 324, 1059
Mauron N., Huggins P.J., 1999, A&A 349, 203
Neugebauer G., Leighton R.B., 1969, Two–Micron Sky Survey – a Preliminary Catalog, NASA SP–3047. Washington, D.C.: Government Printing Office
Osterbart R., Balega Y.Y., Blöcker T., Men'shchikov A.B., Weigelt G., 2000, A&A 357, 169
Reid M.J., Menten K.M., 1997, ApJ 476, 327
Richtmyer R.D., Morton K.W., 1967, Difference methods for initial-value problems, New York: John Wiley & Sons, 2nd edition
Ridgway S.T., Keady J.J., 1988, ApJ 326, 843
Sada P.A.V., 1993, Temporal variations in the circumstellar shell IRC +10216, PhD thesis. New Mexico State University, Las Cruces, New Mexico
Sahai R., 1987, ApJ 318, 809
Schröder K.-P., Winters J.M., Arndt T.U., Sedlmayr E., 1998, A&A 335, L9
Schröder K.-P., Winters J.M., Sedlmayr E., 1999, A&A 349, 898
Skinner C.J., Meixner M., Bobrowsky M., 1998, MNRAS 300, L29
Skinner C., Justtanont K., Tielens A.G.G.M., et al., 1999, MNRAS 302, 293
Truong-Bach, Morris D., Nguyen-Q-Rieu, 1991, A&A 249, 435
Unno W., Kondo M., 1976, PASJ 28, 347
Weigelt G., Balega Y., Blöcker T., et al., 1998, A&A 333, L51
Winters J.M., Dominik C., Sedlmayr E., 1994a, A&A 288, 255
Winters J.M., Fleischer A.J., Gauger A., Sedlmayr E., 1994b, A&A 290, 623
Winters J.M., Fleischer A.J., Gauger A., Sedlmayr E., 1995, A&A 302, 483
Winters J.M., Fleischer A.J., Le Bertre T., Sedlmayr E., 1997, A&A 326, 305
Winters J.M., Le Bertre T., Keady J.J., 1999, in: Le Bertre T., Lèbre A., Waelkens C., IAU Symp. 191: Asymptotic Giant Branch Stars, ASP Conf. Ser, p. 261
Wood P.R., 1979, ApJ 227, 220
Zuckerman B., Dyck H.M., Claussen M.J., 1986, ApJ 304, 401